HHS Public Access

Author manuscript

Nat Microbiol. Author manuscript; available in PMC 2018 November 21.

Published in final edited form as:

Nat Microbiol. 2018 June ; 3(6): 678–686. doi:10.1038/s41564-018-0165-z.

A Unique Cytoplasmic ATPase Complex Defines the *Legionella pneumophila* Type IV Secretion Channel

David Chetrit[*,1], **Bo Hu**[*,2,3], **Peter J. Christie**[2], **Craig R. Roy**[^,1], and **Jun Liu**[^,1,2,3]

[1]Department of Microbial Pathogenesis, Microbial Sciences Institute and Boyer Center for Molecular Medicine, Yale School of Medicine, New Haven, CT 06536 USA

[2]Department of Microbiology and Molecular Genetics, McGovern Medical School, The University of Texas Health Science Center at Houston, Houston, TX 77030 USA

[3]Department of Microbial Pathogenesis and Microbial Sciences Institute, Yale School of Medicine, New Haven, CT 06536 USA, Department of Pathology and Laboratory Medicine, McGovern Medical School, The University of Texas Health Science Center at Houston, Houston, TX 77030 USA

Abstract

Type IV secretion systems (T4SSs) are complex machines used by bacteria to deliver protein and DNA complexes into target host cells [1–5]. Conserved ATPases are essential for T4SS function, but how they coordinate their activities to promote substrate transfer remains poorly understood. Here, we show that the DotB ATPase associates with the Dot/Icm T4SS at the *Legionella* cell pole through interactions with the DotO ATPase. The structure of the Dot/Icm apparatus was solved *in situ* by cryo-electron tomography at 3.5 nanometer resolution and the cytoplasmic complex was solved at 3.0 nanometer resolution. These structures revealed a cell-envelope-spanning channel that connects to the cytoplasmic complex. Further analysis revealed a hexameric assembly of DotO dimers associated with the inner membrane complex, and a DotB hexamer associated with the base of this cytoplasmic complex. The assembly of a DotB/DotO energy complex creates a cytoplasmic channel and directs the translocation of substrates through the T4SS. These data define distinct stages in Dot/Icm machine biogenesis, advance our understanding of channel activation, and identify an envelope-spanning T4SS channel.

Bacteria use Type IV secretion systems (T4SSs) to colonize and proliferate in various clinical and nonclinical settings [1,2]. The T4SSs are complex nanomachines that span the bacterial cell envelope and mediate the delivery of protein and DNA substrates to target cells, a process generally requiring direct cell-to-cell contact [3]. There are two

^Correspondence to: Craig R. Roy craig.roy@yale.edu, Jun Liu jliu@yale.edu.
*These authors contributed equally to this work

Contributions

C.R. and J.L. designed research; D.C. constructed the *L. pneumophila* expression plasmids and strains; B.H. and D.C. collected and together with C.R., J.L. and P.C. analyzed the data; and B.H., C.R., D.C., J.L., and P.C. wrote the paper.

Competing financial interests

The authors declare no competing financial interests.

phylogenetically distinct T4SSs, termed type IVA and IVB. The *Agrobacterium tumefaciens* VirB/VirD4 T4SS and *Escherichia coli* R388 and pKM101 plasmid conjugation systems are IVA systems composed of a dozen different proteins [4]. The IVB systems represented by the *Legionella pneumophila* Dot/Icm T4SS are more complex, requiring more than two dozen proteins [5]. Effector-translocating IVA and IVB systems have three highly conserved ATPases, the substrate receptor VirD4/DotL (also termed the Type IV coupling protein or T4CP), VirB4/DotO, and VirB11/DotB. How these ATPase are structurally arranged at the base of their respective T4SSs to coordinate substrate transfer remains to be determined.

The R388-encoded IVA machine, here designated as the $IVA_{3\text{-}10}$ structure (for the fact that it is composed of homologs of the *A. tumefaciens* VirB3 through VirB10 subunits), was isolated from the *E. coli* cell envelope and the structure was determined by transmission electron microscopy (TEM) [6]. The $IVA_{3\text{-}10}$ structure revealed two large subassemblies, an outer membrane-associated core complex termed the OMCC, which is joined by a thin stalk to an inner membrane complex (IMC). The OMCC is a barrel-shaped structure with dimensions of ~185 Å in width and height that has a central chamber through which substrates presumably pass to the cell exterior. The IMC is unusual in having an asymmetric inner membrane (IM) platform of 255 Å in width and 105 Å in thickness. Associated with the base of this platform are two barrel-shaped hexamers of the VirB4 ATPase, each with dimensions of 135 Å in diameter by 105 Å in length, that project into the cytoplasm. This $IVA_{3\text{-}10}$ structure lacks the VirD4 and VirB11 ATPases, which are components essential for recruitment and delivery of secretion substrates across the IM.

The *L. pneumophila* Dot/Icm T4SS also is composed of an OMCC, originally described as a ring- or barrel-shaped structure reminiscent of the IVA OMCC, but with a much larger cross-section of ~400 Å [7]. Recently, a structure of the Dot/Icm T4SS was revealed in the native context of the *L. pneumophila* cell envelope by cryoelectron tomography (cryo-ET) [8]. The OMCC visualized *in situ* displayed two distinct curved layers, the larger just below the outer membrane (OM) and the smaller in the periplasm. This structure was designated as “WiFi-like” and is composed of at least 5 subunits, DotC, DotD, DotF, DotG, and DotH. An IMC was observed at lower resolution. A side-view image of the IMC identified 4 rod-like structures extending into the cytoplasm. Based on their overall dimensions and positions with respect to the IM and OMCC, and by analogy to the $IVA_{3\text{-}10}$ structure, these projections might represent the walls of two barrel-shaped hexamers of the DotO ATPase.

Fundamental questions remain about how IVA and IVB system are architecturally configured and translocate substrates, particularly across the cytoplasmic membrane. Here, fluorescence microscopy was combined with a high-throughput cryo-ET pipeline to investigate the *L. pneumophila* Dot/Icm system. These data demonstrate the association of the DotB ATPase with the T4SS, and reveal that the cytoplasmic complex is composed of an ATPase subassembly. Remarkably, the cytoplasmic complex of this IVB system is highly symmetric with two hexamers of DotB and DotO stacked on one another and centrally positioned at the base of an IM-spanning channel. Consequently, in contrast to the asymmetric $IVA_{3\text{-}10}$ structure [6], the IVB structure lends itself readily to the visualization of a translocation pathway by which substrates recruited to the base of the secretion apparatus are conveyed from the bacterial cytosol through a continuous channel to the cell surface.

DotB association with the polar Dot/Icm machine

The Dot/Icm system assembles at cell division sites and localizes at the bacterial poles [9]. To investigate the requirements for polar-positioning and characterize dynamic features associated with machine biogenesis, genes encoding sfGFP or mCherry were fused to *dot* and *icm* genes and recombined at their native positions on the chromosome. This approach preserved both the stoichiometry and timing of fusion protein production relative to the other Dot/Icm machine subunits.

The OMCC is composed of three OM-associated proteins, the DotC and DotD lipoproteins and DotH, and two large proteins, DotF and DotG, that extend from the IM across the periplasm to form contacts with the DotC/D/H subassembly (Fig. 1a) [7,10]. We confirmed that fluorescently-tagged OMCC subunit DotG-sfGFP, the IMC subunit DotI-sfGFP, the T4CP subunit DotL-sfGFP, cytoplasmic secretion ATPase DotB-sfGFP and the secretion chaperone IcmS-sfGFP were produced as stable and functional components as monitored by immunoblot analysis and a Dot/Icm-dependent intracellular growth assay (Supplementary information Fig. 1a,b). As predicted, DotG-sfGFP and DotL-sfGFP localized at the cell poles (Fig. 1b). By contrast, IcmS-sfGFP was distributed throughout the cytosol, and DotB-sfGFP was polar-localized only in a subset of cells (Fig. 1b). Polarity scores that indicate the ratio of fluorescence measured at the poles compared to fluorescence measured near the middle of the cell were determined for individual cells. The majority of cells producing DotB-sfGFP had a lower polarity score compared to cells producing either DotG-sfGFP or DotL-sfGFP (Fig 1b; Supplementary information Fig. 1c). Furthermore, time-lapse videos revealed that DotB-sfGFP displayed cytosolic movement in most bacterial cells (Supplementary information Video 1), indicating that this ATPase is present in a dynamic cytosolic population but is also capable of associating with the polar Dot/Icm complex. Similar to DotG-sfGFP fluorescence, DotB-sfGFP fluorescence at the poles did not recover rapidly after photobleaching, whereas the fluorescence of cytosolic DotB-sfGFP and soluble sfGFP alone recovered rapidly (Fig. 1c,d). Thus, the assembled Dot/Icm machine creates a stable complex localized at the cell poles, and the DotB protein is present as a dynamic entity in the cytosol that is capable of polar association.

DotB mutations that confer defects on ATP binding or hydrolysis were used to determine how ATP-dependent movement of this energizing factor might impact DotB cellular localization (Fig. 1e) [11]. All but one of the mutations severely impaired polar recruitment of DotB, which indicated that ATP catalysis was important for polar positioning (Fig. 1f,g). The notable exception, $DotB_{E191K}$, was previously reported to bind but not hydrolyze ATP [11]. The $DotB_{E191K}$-sfGFP variant localized almost exclusively at cell poles (Fig. 1f,g) and was significantly less dynamic compared to native DotB-sfGFP (Supplementary information Fig. 1d & Video 1). This indicated that ATP-bound DotB protein associates stably with the Dot/Icm machine at cell poles (see also below).

Polar-positioned DotO ATPase recruits DotB

To define the requirements of the Dot/Icm machine for DotB polar localization, individual *dot* or *icm* genes were deleted to assess effects on $DotB_{E191K}$-sfGFP positioning (Fig. 2a,b).

Deletions that eliminated production of essential OMCC subunits, DotC, DotD, and DotG, but not the nonessential core subunit DotF or the periplasmic protein DotK, abolished polar localization of $DotB_{E191K}$-sfGFP. Similarly, deletions that eliminated production of most IMC components (DotJ, IcmT, IcmV, IcmQ, DotI, DotU, DotE, DotA) strongly abrogated $DotB_{E191K}$-sfGFP polar localization. Elimination of the IM subunits DotP or DotV had less severe effects on $DotB_{E191K}$-sfGFP localization, possibly because these subunits play ancillary roles in machine biogenesis. Among the cytosolic IVB components, only the Δ*dotO* mutation eliminated $DotB_{E191K}$-sfGFP polar localization, consistent with the DotO ATPase having an essential role in the docking of DotB to the IVB apparatus. By contrast, deletions of the T4CP DotL and components of the associated effector-binding adapter complex (DotM, DotN, IcmW, LvgA) [12–14] did not have a dramatic effect on $DotB_{E191K}$-sfGFP polar localization, arguing against a role for this cytoplasmic subassembly in DotB recruitment. Deletions of the entire Dot/Icm system or of essential OMCC (DotG, DotD) or IMC (DotU, DotA) subunits abrogated polar positioning of native DotB (Supplementary information Fig. 2a), confirming the importance of the Dot/Icm machine for recruitment of this ATPase.

The possible role of DotO in recruitment of DotB to the polar-localized Dot/Icm T4SS was evaluated further. As shown for $DotB_{E191K}$-sfGFP and in contrast to DotB-sfGFP, DotO-sfGFP was positioned at the cell poles and was static (Fig. 2c,d). The OMCC subunit DotG and the IMC subunits DotI or DotU were essential for polar recruitment of DotO-sfGFP or DotO-mCherry (Fig. 3a,b, Supplementary information Fig. 2b). By contrast, deletion of the DotB or DotL ATPases had no effect on DotO-sfGFP polar positioning (Fig. 3a,b). Thus, DotO recruitment to cell poles requires a Dot/Icm platform containing the OMCC and IMC, but does not require the ATPases DotB or DotL (Fig 3c). Additional studies supported a model where DotO recruits DotB to Dot/Icm machines at the cell pole. In cells coproducing DotO-mCherry and $DotB_{E191K}$-sfGFP, tagged DotO localized to the cell pole but tagged $DotB_{E191K}$ did not (Fig. 3d,e). As expected from our above findings, DotL-mCherry had no effect on polar localization of tagged $DotB_{E191K}$-sfGFP (Fig. 3d,e). Thus, addition of mCherry specifically to the C-terminus of DotO impeded DotB recruitment to the T4SS, suggestive of a steric effect in blocking a DotO-DotB interaction. Further evidence for a DotB-DotO interaction was gained by immunoprecipitation, in which GFP-specific antibodies co-precipitated DotO in a complex containing DotB-sfGFP or $DotB_{E191K}$-sfGFP (Supplementary information Fig. 2c).

These studies support a biogenesis pathway in which the Dot/Icm T4SS assembles at the *L. pneumophila* cell poles, first, by formation of a stable OMCC/IMC substructure that spans the entire cell envelope, and next, by recruitment of the DotO ATPase. When positioned, DotO recruits the ATP-bound form of DotB, likely in response to channel-activating signals that are presently not specified.

Dot/Icm structure revealed by cryo-ET

To define the spatial organization of the IVB-encoded ATPases relative to each other and the IVB channel, high-throughput cryo-ET was used to visualize the intact Dot/Icm system in wild type and mutant cells. A typical reconstruction of a *L. pneumophila* cell revealed

multiple cone-shaped complexes embedded in the cell envelope (Fig. 4a, Supplementary information Video 2). These cone-shaped structures resemble the previously observed polar-localized Dot/Icm subassemblies [8,9]. We identified 3,314 cone-shaped complexes from 771 tomographic reconstructions of the cell tips. Sub-tomogram averaging was then utilized to determine the overall structure of the intact IVB machine at a resolution of 3.5 nm (Supplementary information Fig. 3). In the resulting images, the envelope-spanning Dot/Icm machine was shown to consist of two large subassemblies, a distinct OMCC and a cytoplasmic complex (Fig. 4b).

The OMCC is approximately 42 nm in width and 31 nm in height, and further refinement revealed important details that were not apparent in previous structures [8]. The top portion of this subassembly, incorporated in the OM, adopts a wheel-like structure with 13-fold symmetry (Fig. 4c, Supplementary information Fig. 3). The entire wheel-like structure is embedded in the inner leaflet of the OM and establishes intimate contacts with the outer leaflet of the OM (Fig. 4c, Supplementary information Fig. 3j-m). Association of the wheel-like structure also appears to locally remodel the OM (Fig. 4a, b). The wheel has a central pore of ~6 nm in diameter that projects across the outer leaflet of the OM (Fig. 4c, Supplementary information Fig. 3). The wheel extends into the periplasm to the peptidoglycan (PG), where it is connected to a cylinder of ~20 nm in diameter and with a central channel of ~6 nm at the connection point (Fig. 4b-f). As the cylinder extends to the IM, however, it abruptly narrows to a diameter of ~10 nm and a channel of ~3 nm (Fig. 4b, Supplementary information Fig. 3). Another striking feature of the OMCC is the presence of a plug domain of ~25 nm in length that extends through the center of the wheel beginning at the OM and extending through the center of the cylinder to the point of abrupt narrowing (Fig. 4b,e,f). A collar also surrounds the cylinder that extends from the IM to the PG layer (Fig. 4d,e). These features are displayed clearly in three-dimensional (3-D) reconstructions: a side view of the intact T4SS (Fig. 4d), a cross-section view showing the architectural features (Fig. 4e), and an end-on view showing the 13-fold symmetry of the wheel and OM pore with the interior plug possibly functioning as a regulatory gate (Fig. 4f).

DotG, a central channel subunit

DotG extends from the IM to the OMCC subassembly [7,10]. To determine the structural contribution of DotG to Dot/Icm machine architecture, 3-D reconstructions of machines produced in a Δ*dotG* mutant strain were obtained. The Δ*dotG* mutation is nonpolar on downstream gene expression, as shown by *trans*-complementation with the native *dotG* [10]. The Δ*dotG* mutant machines were detectable at *L. pneumophila* cell poles (Supplementary information Fig. 4, Video 2) and also retained the ability to assemble wheel-shaped OMCC complexes with 13-fold symmetry (Supplementary information Fig. 4). However, the mutant machines differed from the WT machines in two pronounced ways. First, among the Δ*dotG* mutant machines examined (374 cone-shaped complexes from 96 tomographic reconstructions), the distance between OM and IM varied from 26 - 33 nm, in contrast to a more fixed dimension of ~30 nm observed for cells producing the WT machine (Supplementary information Fig. 4). Second, the Δ*dotG* machines lacked most of the cylinder that in the WT machines extends from the OM wheel to the IM (Supplementary information Fig. 4). This was evidenced both by a lack of cylinder density in a side-view and

an end-on view (Supplementary information Fig. 4). These findings indicate that DotG physically couples the OMCC with the cytoplasmic complex by forming the portion of the central channel corresponding to the cylinder domain (see Fig. 4e).

A DotO/DotB ATPase subassembly

To characterize the cytoplasmic complex, the *in situ* structures of the WT and mutant T4SS machines lacking each of the 3 ATPases (DotO, DotB, DotL) were compared. In the WT machine, two ring-like discs with diameters of 16 nm and 27 nm were detected at the base of the IM (Fig. 5a,g, Supplementary information Fig. 5). Further refinement of the cytoplasmic complex at 3.0 nm resolution revealed inverted V-shaped structures of 32 nm in width and 24 nm in length connected to the IM portion of the complex (Fig. 5b,h). The cytoplasmic complex consists of 6 V-shaped structures with the inner arms interacting to form a hexamer, and the outer arms splaying away from the hexamer in a rosette pattern (Fig. 5h,l,m). The apex of the V-shaped is associated with the IM, and the distal tips of the inner arms are connected to a thin disc (Fig. 5b) that in the end-on view forms a central channel (Fig. 5m). Notably, in the side view the V-shaped structures formally resemble the rod-like appendages that were previously reported to extend into the cytoplasm at the base of the Dot/Icm machine [8]. Although these were interpreted to correspond to the sides of two hexamers of the DotO ATPase by analogy to the type IVA $VirB_{3-10}$ structure, data here clearly establish that 6 of these V-shaped structures instead form a single concentric ring at the base of the Dot/Icm machine.

The Δ*dotB* mutant machines (1,571 cone-shaped complexes from 171 tomographic reconstructions) lacked the disc positioned at the base of the WT machine (compare Fig. 5b,h to Fig. 5d,j). To further evaluate whether DotB contributes directly to this disc, the structure of the cytoplasmic complex was determined using a Δ*dotB* strain producing $DotB_{E191K}$-sfGFP (2,290 cone-shaped complexes from 449 tomographic reconstructions). Remarkably, the density that was missing at the base of cytoplasmic complex in the Δ*dotB* mutant reappeared in the strain producing the $DotB_{E191K}$-sfGFP protein, and an extra density was detected that correlated with the additional mass of sfGFP (Fig. 5c,i). Thus, the disc positioned at the base of the cytoplasmic complex is a DotB hexamer (Fig. 5k).

Significantly, the Δ*dotO* mutant machines (1,513 cone-shaped complexes from 251 tomographic reconstructions) completely lacked the V-shaped structures and associated central disc shown above to correspond to DotB (Fig. 5f, Supplementary information Fig. 5). These findings, coupled with the imaging studies showing that DotO recruits DotB to IVB machines at the pole, strongly implicate DotO as the membrane proximal component of the cytoplasmic complex. Previous studies have shown that VirB4-like subunits assemble both as dimers and hexamers and that their N-proximal domains mediate contacts with the IM [15–18]. Thus, the V-shaped structures most likely correspond to two DotO subunits connected to each other and to the IM platform via their N-terminal domains. In the 3-D model, the C-terminal domains of DotO extend into the cytoplasm (Fig. 5k). In support of this configuration, the atomic structures of a C-terminal domain of a VirB4 homolog [19] fit well within the densities comprising the proximal halves of the V arms (Fig. 5 l,m). An interesting and unique feature of this structure is that the presumptive DotO subunits

comprising the V inner arms interact laterally to form a central hexamer. Accordingly, we present the central channel positioned at the base of the Dot/Icm T4SS as a DotO hexamer comprised of 6 dimers. The cytoplasmic complex therefore consists of two stacked hexamers, one of DotO assembled as a hexamer of dimers and the second of DotB, positioned at the entrance to the Dot/Icm channel (Supplementary information Video 2).

No density corresponding to the large DotL - adaptor complex [14] was apparent in this solved structure. To further evaluate whether the DotL-adaptor complex contributes to assembly of the cytoplasmic complex, we visualized machines in a Δ*dotL* mutant. Deletion of *dotL* is normally toxic to *L. pneumophila*, but this toxicity can be suppressed by loss-of-function mutations in other *dot* or *icm* genes[20]. Accordingly, the Δ*dotL* mutation was constructed in a strain producing the non-functional $DotB_{E191K}$-sfGFP protein. The Δ*dotL* mutant machines (864 cone-shaped complexes from 160 tomographic reconstructions) showed no discernible differences in the cytoplasmic complex compared with the functional Dot/Icm machines in strains producing DotB-sfGFP (compare Fig. 5e and Fig. 5c). These findings confirm that the DotL-adaptor complex is neither a stable component nor necessary for assembly of the cytoplasmic structure. The association of the DotL-adaptor complex with the Dot/Icm machine might be transient and mediated by effector binding or other intracellular or extracellular signals.

Summary

Here, complementary cell imaging and cryo-ET were used to define the dynamics and architecture of the DotB/DotO energy complex at the base of the Dot/Icm channel. Our cell imaging data identified a late-stage assembly reaction in which the spatially dynamic DotB ATPase is recruited to the polar-localized Dot/Icm T4SS (Supplementary information Video 1), presumably to activate the T4SS for transport. The 3-D structure of the intact Dot/Icm system revealed striking details about the OMCC and also identified a cytoplasmic complex comprised of hexamers of DotB and DotO (Supplementary information Video 2). The OMCC has 13-fold symmetry, an OM pore, and a central channel that extends along its length to the IM platform. In line with functions ascribed to other VirB10-like subunits, DotG links the OMCC to the cytoplasmic complex and may also comprise part of the central channel in the periplasm named here as the cylinder. The cytoplasmic complex displayed 6-fold symmetry due to the stacked configuration of the DotO and DotB hexamers. Significantly, despite the mismatch in OMCC/cytoplasmic symmetries (Supplementary information Fig. 6), the Dot/Icm IVB structure overall is highly symmetrical. This is in contrast to the solved IVA structure of the $VirB_{3\text{-}10}$ complex, whose IMC is asymmetric and marked by the presence of two side-by-side VirB4 hexamers and whose connection to the symmetrical OMCC is structurally undefined (Supplementary information Fig. 6) [6]. Our structure therefore offers for the first time an architectural rendering of the entire route by which substrates are conveyed through a T4SS, beginning with the recruitment of substrates to the DotB/DotO energy complex at the channel entrance and ending with their passage across the OM through a pore formed by the distal wheel of the OMCC (Supplementary information Fig. 7).

T4SSs translocate substrates in response to activating signals conveyed upon contact with target cells. Certain architectural features of the central channel, e.g., constrictions within the hexameric ATPases and the periplasmic cylinder and the large plug domain extending across the wheel/cylinder interface (Figs. 4, 5), thus might undergo signal-activated conformational transitions to regulate substrate passage through the T4SS. Activating signals also likely stimulate recruitment of the DotB ATPase to the Dot/Icm T4SS, as well as the recently-described DotL-adaptor complex [13,14] that was not detected in the *in situ* structure. In the activated Dot/Icm machine, the DotL-adaptor complex might position adjacent to the Dot/Icm T4SS where its long, C-terminal extension acts as a flexible arm to feed substrates to the DotB/DotO channel entrance (Supplementary information Fig. 7).

This work describes dynamic features of T4SS machine assembly, presents an *in situ* structure of a T4SS in unprecedented detail, and facilitates a better understanding of the substrate translocation route through a T4SS. Our findings form a solid foundation for further studies aimed at defining further mechanistic and structural details of type IV secretion. The T4SSs are widely used not just for interkingdom transfer of effector proteins, but also for dissemination of genetic material including antibiotic resistance genes between bacteria. The dynamic and structural features of the Dot/Icm system identified here thus represent viable targets for the development of intervention strategies aimed at suppressing pathogenic potential as well as the spread of antibiotic resistance.

Methods

Bacterial strains and plasmids

Bacterial strains used in this study are derived from *L. pneumophila* strains LP01 and LP02 and are listed in Table S1. *L. pneumophila* was grown on charcoal yeast extract (CYE) plates in 37 °C as described previously [21]. *L. pneumophila* strains were constructed by standard recombinant DNA and allelic exchange procedures using the plasmid pSR47S as described previously [22]. sfGFP or mCherry were inserted downstream the Dot/Icm genes and separated by a DNA linker encoding Arg-Thr-Gly-Gly-Ala-Ala.

Fluorescent microscopy imaging and processing

Imaging of *L. pneumophila* expressing Dot/Icm fluorescent fusions was carried out by resuspension of 2 day heavy patches in water, after which they were spotted on a thin pad of 1% agarose, covered with a cover slip and immediately imaged at room temperature. Fluorescence micrographs were captured using a Nikon Eclipse TE2000-S inverted microscope equipped with a Spectra X light engine from Lumencor, CoolSNAP EZ 20MHz digital monochrome camera from Photometrics and a Nikon Plan Apo100× objective len (1.4 numerical aperture) under the control of SlideBook™ 6.0 (Intelligent Imaging Innovations). Samples were imaged using a 196 mW 485 nm or a 260 mW 560 nm LED lights, with typical exposure times of 100-400 ms and 2×2 binning. Time lapses of DotB-sfGFP were acquired using continuous illumination. Polarity scores were calculated with SlideBook™ by measuring the ratio between the variance and the mean of the fluorescence signal at region of interest located between the pole and the cell center [22]. DotB-sfGFP and DotO-sfGFP time laps micrographs (Figure 2C) were acquired using a Nikon TE2000

spinning disc confocal microscope equipped with a Nikon Plan Apo100× objective (1.4 numerical aperture) and restored by the NearestNeighbors deconvolution algorithm [23] of SlideBook™. Fluorescent recovery after photobleaching FRAP was performed on a Nikon TiE by fiber coupling a 405-nm solid state laser into the FRAP arm of a TIRF/FRAP illuminator, which focuses the laser to a single diffraction-limited spot on the sample. Imaging was accomplished in wide-field by illuminating the sample with the 470/24 line of a SpectraX solid-state light source laser delivering a wavelength of 405 nm. The photobleached area was determined with SlideBook™ software; bleaching was achieved with minimal intensities to avoid possible phototoxic effects. Fluorescence intensity measurements were corrected for non-specific photobleaching. The premise for the correction is that the overall intensity of non-bleached areas (of different cells in the same field) should remain constant over time. Intensity measurements were multiplied by the inverse of the ratio of fluorescence at a given time point over fluorescence at the initial time point.

Intracellular growth assay

Replication of *L. pneumophila* in RAW 264.7 macrophage-like cells was determined over 2 days using a standard assay that has been described previously [37]. Briefly, RAW 264.7 macrophage-like cells in 24 well tissue culture dishes were infected with *L. pneumophila* at a multiplicity of infection of 1. One hour after infection the wells were washed with PBS and fresh tissue culture medium was added to each wells. Colony-forming units were determined from individual wells after the PBS washes and at 2-days to measure intracellular replication.

Immunoblot analysis and co-immunoprecipitation

For immunoblot analysis, *L. pneumophila* cultures were grown for 48 h at 37 °C on CYE plates, resuspended in water and adjusted to an OD_{600} of 1.2. Cells from 300 μl were collected by centrifugation at 21,000g for 1 min and resuspended in 300 μl Laemmli sample buffer and boiled for 10 min. 15 μl were loaded for western blot analysis using a primary polyclonal anti GFP antibody (GenScript) followed by incubation with secondary antibody conjugated to horseradish peroxidase (Sigma). Proteins were visualized by using an ECL detection kit (Amersham Biosciences). For co-immunoprecipitation analysis, *L. pneumophila* cultures were grown for 48 h at 37 °C on CYE plates. Cultures were resuspended in water and adjusted to an OD_{600} of 6. Cells from 10 ml were collected by centrifugation at 11,000g for 10 min, re-suspended in 1.5 ml of in lysis buffer (50 mM Tris-HCl pH 8) with protease inhibitor cocktail (Roche Diagnostics), EDTA (2mM) and lysozyme (0.2 mg ml^{-1}, Sigma) and incubated for 1 h on ice prior to sonication. Lysates were centrifuged 10 min at 10,000 g and filtered to remove unlysed cells before the supernatant was incubated for 1 h at 4 °C with a polyclonal anti GFP antibody (GenScript). Samples were then incubated over night with protein A magnetic beads (Novex) and washed 10 times with the lysis buffer. Finally, beads, were resuspended in 30 μl Laemmli sample buffer and boiled for 10 min. 10 μl were loaded for western blot analysis using a primary polyclonal anti DotO antibody (provided by Ralph Isberg).

Preparation of Frozen-Hydrated Specimens

Bacterial cultures were grown 48 h at 37 °C on CYE agar plates. Bacteria were removed from the plates and suspended in water, then mixed with 10 nm colloidal gold particles (used as fiducial markers in image alignment) and deposited onto freshly glow-discharged, holey carbon grids for 1 min. The grids were blotted with filter paper and rapidly frozen in liquid ethane, using a gravity-driven plunger apparatus as described previously [24,25].

Cryo-ET Data Collection and 3-D Reconstructions

The frozen-hydrated specimens were imaged at −170 °C using a Polara G2 electron microscope (FEI Company) equipped with a field emission gun and a direct detection device (Gatan K2 Summit). The microscope was operated at 300 kV with a magnification of ×15,500, resulting in an effective pixel size of 2.5 Å at the specimen level. We used SerialEM [26] to collect low-dose, single-axis tilt series with dose fractionation mode at about 5 μm defocus and a cumulative dose of ~50 $e^{-}/Å^{2}$ distributed over 35 stacks. Each stack contains ~8 images. Over 2,000 tilt series were collected from −51° to 51° with increment of 3°. We used Tomoauto [25] to facilitate data processing which includes drift correction of dose-fractionated data using Motioncorr [27] and assembly of corrected sums into tilt series, automatic fiducial seed model generation, alignment and contrast transfer function correction of tilt series by IMOD [28], and reconstruction of tilt series into tomograms by Tomo3D [29]. Each tomographic reconstruction is 3,710 × 3,838 × 2,400 pixels and ~130Gb in size. In total, 2,062 tomographic reconstructions from 7 different strains were generated (Supplementary Information Table 2).

Sub-tomogram averaging and correspondence analysis

We used tomographic package I3 (0.9.9) for sub-tomogram analysis as described previously [30]. A total of 10,291 Type IVB secretion machines (400 × 400 × 400 voxels) were visually identified and then extracted from 2,062 cryo-tomographic reconstructions. Two of the three Euler angles of each Type IVB secretion machine were estimated based on the orientation of each particle in the cell envelope. To accelerate image analysis, 4×4×4 binned sub-tomograms (100×100×100 voxels) were used for initial alignment. The alignment proceeds iteratively with each iteration consisting of three parts in which references and classification masks are generated, sub-tomograms are aligned and classified, and finally class averages are aligned to each other. Classification focusing on core complex showed 13-fold symmetry feature, so in the following processing a 13-fold symmetry was imposed to assist the sub-tomograms alignment. Further classification focusing on the cytoplasmic complex showed a hexagonal structure in four different classes. After multiple cycles of alignment and classification for 4×4×4 binned sub-tomograms, we used 2×2×2 binned sub-tomograms for refinement. Fourier shell correlation (FSC) between the two independent reconstructions was used to estimate the resolution of the averaged structures (Supplementary Information Fig. 4).

3-D Visualization and Molecular Modeling

We used IMOD to visualize the maps and also to generate 3-D surface rendering of *L. pneumophila* cell and UCSF Chimera [31] to visualize subtomogram averages in 3-D and

molecular modeling. The pseudo DotO C-terminal structure was modeled using VirB4 (PDB 4AG5) as template, each of 12 DotO C-terminal structures was manually fitted onto the each of distal half of 12 rods. Since no DotB structure is available, we used a homohexamer of PilT (PDB 3JVV) fit into the distal short cylinder with its C terminal toward cytoplasm.

Statistical analysis

All experiments were performed at least twice, unless otherwise noted. Differences in the distribution of polarity scores were determined using a non-parametric test (Mann–Whitney), as most of samples displayed long tailed distributions. $P < 0.05$ was considered significant. For most microscopy experiments, roughly 200 cells were analyzed. For FRAP experiments means were compared using a two-sided Student's t-test. No statistical methods were used to predetermine sample size, and the researchers were not blinded to sample identity.

Data Availability

Density maps and coordinate data that support the Dot/Icm structure determined by cryo-ET have been deposited in EMDB (EMD-7611, EMD-7612). The authors declare that all other data supporting the findings of this study are available within the paper and its supplementary information files.

Supplementary Material

Refer to Web version on PubMed Central for supplementary material.

Acknowledgments

B.H. and J.L were supported by the National Institutes of Health (R01AI087946 and R01GM107629) and the Welch Foundation (AU-1714). D.C. and C.R. were supported by the NIH (R37AI041699 and R21AI130671). P.C. was supported by the NIH (R01GM48476). We are grateful to S.S. Ivanov (Louisiana State University) for insightful suggestions and critique; H. Nagai (Gifu University) for the *L. pneumophila* Δ*T4SS* strain; R.R. Isberg (Tufts University) for the antibody to DotO; E.H. Rego (Yale University) for technical assistance with FRAP.

References

1. Christie PJ, Whitaker N, Gonzalez-Rivera C. Mechanism and structure of the bacterial type IV secretion systems. Biochim Biophys Acta. 2014; 1843:1578–1591. DOI: 10.1016/j.bbamcr.2013.12.019 [PubMed: 24389247]
2. Gonzalez-Rivera C, Bhatty M, Christie PJ. Mechanism and function of type IV secretion during infection of the human host. Microbiol Spectr. 2016; 4
3. Costa TR, et al. Secretion systems in Gram-negative bacteria: structural and mechanistic insights. Nat Rev Microbiol. 2015; 13:343–359. DOI: 10.1038/nrmicro3456 [PubMed: 25978706]
4. Trokter M, Felisberto-Rodrigues C, Christie PJ, Waksman G. Recent advances in the structural and molecular biology of type IV secretion systems. Curr Opin Struct Biol. 2014; 27:16–23. DOI: 10.1016/j.sbi.2014.02.006 [PubMed: 24709394]
5. Kubori T, Nagai H. The type IVB secretion system: an enigmatic chimera. Curr Opin Microbiol. 2015; 29:22–29. DOI: 10.1016/j.mib.2015.10.001 [PubMed: 26529574]
6. Low HH, et al. Structure of a type IV secretion system. Nature. 2014; 508:550–553. DOI: 10.1038/nature13081 [PubMed: 24670658]

7. Kubori T, et al. Native structure of a type IV secretion system core complex essential for Legionella pathogenesis. Proc Natl Acad Sci U S A. 2014; 111:11804–11809. DOI: 10.1073/pnas.1404506111 [PubMed: 25062693]
8. Ghosal D, Chang YW, Jeong KC, Vogel JP, Jensen GJ. *In situ* structure of the Legionella Dot/Icm type IV secretion system by electron cryotomography. EMBO Rep. 2017; 18:726–732. DOI: 10.15252/embr.201643598 [PubMed: 28336774]
9. Jeong KC, Ghosal D, Chang YW, Jensen GJ, Vogel JP. Polar delivery of Legionella type IV secretion system substrates is essential for virulence. Proc Natl Acad Sci U S A. 2017; 114:8077–8082. DOI: 10.1073/pnas.1621438114 [PubMed: 28696299]
10. Vincent CD, et al. Identification of the core transmembrane complex of the *Legionella* Dot/Icm type IV secretion system. Mol Microbiol. 2006; 62:1278–1291. [PubMed: 17040490]
11. Sexton JA, Yeo HJ, Vogel JP. Genetic analysis of the Legionella pneumophila DotB ATPase reveals a role in type IV secretion system protein export. Mol Microbiol. 2005; 57:70–84. DOI: 10.1111/j.1365-2958.2005.04667.x [PubMed: 15948950]
12. Sutherland MC, Nguyen TL, Tseng V, Vogel JP. The Legionella IcmSW complex directly interacts with DotL to mediate translocation of adaptor-dependent substrates. PLoS Path. 2012; 8:e1002910.
13. Vincent CD, Friedman JR, Jeong KC, Sutherland MC, Vogel JP. Identification of the DotL coupling protein subcomplex of the Legionella Dot/Icm type IV secretion system. Mol Microbiol. 2012; 85:378–391. DOI: 10.1111/j.1365-2958.2012.08118.x [PubMed: 22694730]
14. Kwak MJ, et al. Architecture of the type IV coupling protein complex of *Legionella pneumophila*. Nat Microbiol. 2017; 2:17114. [PubMed: 28714967]
15. Dang TA, Christie PJ. The VirB4 ATPase of *Agrobacterium tumefaciens* is a cytoplasmic membrane protein exposed at the periplasmic surface. J Bacteriol. 1997; 179:453–462. [PubMed: 8990298]
16. Dang TA, Zhou XR, Graf B, Christie PJ. Dimerization of the *Agrobacterium tumefaciens* VirB4 ATPase and the effect of ATP-binding cassette mutations on the assembly and function of the T-DNA transporter. Mol Microbiol. 1999; 32:1239–1253. [PubMed: 10383764]
17. Durand E, Oomen C, Waksman G. Biochemical dissection of the ATPase TraB, the VirB4 homologue of the *Escherichia coli* pKM101 conjugation machinery. J Bacteriol. 2010; 192:2315–2323. DOI: 10.1128/JB.01384-09 [PubMed: 20172994]
18. Durand E, Waksman G, Receveur-Brechot V. Structural insights into the membrane-extracted dimeric form of the ATPase TraB from the *Escherichia coli* pKM101 conjugation system. BMC Struct Biol. 2011; 11:4. [PubMed: 21266026]
19. Wallden K, et al. Structure of the VirB4 ATPase, alone and bound to the core complex of a type IV secretion system. Proc Natl Acad Sci U S A. 2012; 109:11348–11353. DOI: 10.1073/pnas.1201428109 [PubMed: 22745169]
20. Roy CR, Isberg RR. Topology of *Legionella pneumophila* DotA: an inner membrane protein required for replication in macrophages. Infect Immun. 1997; 65:571–578. [PubMed: 9009315]
21. Buscher BA, et al. The DotL protein, a member of the TraG-coupling protein family, is essential for viability of Legionella pneumophila strain Lp02. J Bacteriol. 187:2927–2938.
22. Merriam JJ, Mathur R, Maxfield-Boumil R, Isberg RR. Analysis of the *Legionella pneumophila fliI* gene: intracellular growth of a defined mutant defective for flagellum biosynthesis. Infect Immun. 1997; 65:2497–2501. [PubMed: 9169800]
23. Chetrit D, et al. Negative regulation of the endocytic adaptor disabled-2 (Dab2) in mitosis. J Biol Chem. 2011; 286:5392–5403. DOI: 10.1074/jbc.M110.161851 [PubMed: 21097498]
24. Hu B, Lara-Tejero M, Kong Q, Galan JE, Liu J. *In situ* molecular architecture of the Salmonella type III secretion machine. Cell. 2017; 168:1065–1074 e1010. DOI: 10.1016/j.cell.2017.02.022 [PubMed: 28283062]
25. Morado DR, Hu B, Liu J. Using Tomoauto: A protocol for high-throughput automated cryo-electron tomography. J Vis Exp. 2016:e53608. [PubMed: 26863591]
26. Mastronarde DN. Automated electron microscope tomography using robust prediction of specimen movements. J Struct Biol. 2005; 152:36–51. DOI: 10.1016/j.jsb.2005.07.007 [PubMed: 16182563]

27. Li X, et al. Electron counting and beam-induced motion correction enable near-atomic-resolution single-particle cryo-EM. Nat Methods. 2013; 10:584–590. DOI: 10.1038/nmeth.2472 [PubMed: 23644547]
28. Kremer JR, Mastronarde DN, McIntosh JR. Computer visualization of three-dimensional image data using IMOD. J Struct Biol. 1996; 116:71–76. DOI: 10.1006/jsbi.1996.0013 [PubMed: 8742726]
29. Agulleiro JI, Fernandez JJ. Tomo3D 2.0–exploitation of advanced vector extensions (AVX) for 3D reconstruction. J Struct Biol. 2015; 189:147–152. DOI: 10.1016/j.jsb.2014.11.009 [PubMed: 25528570]
30. Hu B, et al. Visualization of the type III secretion sorting platform of *Shigella flexneri*. Proc Natl Acad Sci U S A. 2015; 112:1047–1052. DOI: 10.1073/pnas.1411610112 [PubMed: 25583506]
31. Pettersen EF, et al. UCSF Chimera–a visualization system for exploratory research and analysis. J Comput Chem. 2004; 25:1605–1612. DOI: 10.1002/jcc.20084 [PubMed: 15264254]
32. Agard DA, Hiraoka Y, Shaw P, Sedat JW. Fluorescence microscopy in three dimensions. Methods Cell Biol. 1989; 30:353–377. [PubMed: 2494418]
33. Frick-Cheng AE, et al. Molecular and structural analysis of the *Helicobacter pylori cag* type IV secretion system core complex. MBio. 2016; 7:e02001–02015. DOI: 10.1128/mBio.02001-15 [PubMed: 26758182]
34. Berger KH, Isberg RR. Two distinct defects in intracellular growth complemented by a single genetic locus in *Legionella pneumophila.* Mol Microbiol. 1993; 7:7–19. [PubMed: 8382332]
35. Andrews HL, Vogel JP, Isberg RR. Identification of linked Legionella pneumophila genes essential for intracellular growth evasion of the endocytic pathway. Infect Immun. 1998; 66:950–958. [PubMed: 9488381]
36. Vogel JP, Andrews HL, Wong SK, Isberg RR. Conjugative transfer by the virulence system of *Legionella pneumophila*. Science. 1998; 279:873–876. [PubMed: 9452389]
37. Zuckman DM, Hung JB, Roy CR. Pore-forming activity is not sufficient for *Legionella pneumophila* phagosome trafficking and intracellular growth. Mol Microbiol. 1999; 32:990–1001. [PubMed: 10361301]
38. Finan TM, Kunkel B, De Vos GF, Signer ER. Second symbiotic megaplasmid in *Rhizobium meliloti* carrying exopolysaccharide and thiamine synthesis genes. J Bacteriol. 1986; 167:66–72. [PubMed: 3013840]

Author Manuscript

Author Manuscript

Author Manuscript

One sentence summary

Characterization of a DotO/DotB ATPase energy complex at the base of the Dot/Icm system defines the route of T4SS substrate transfer.

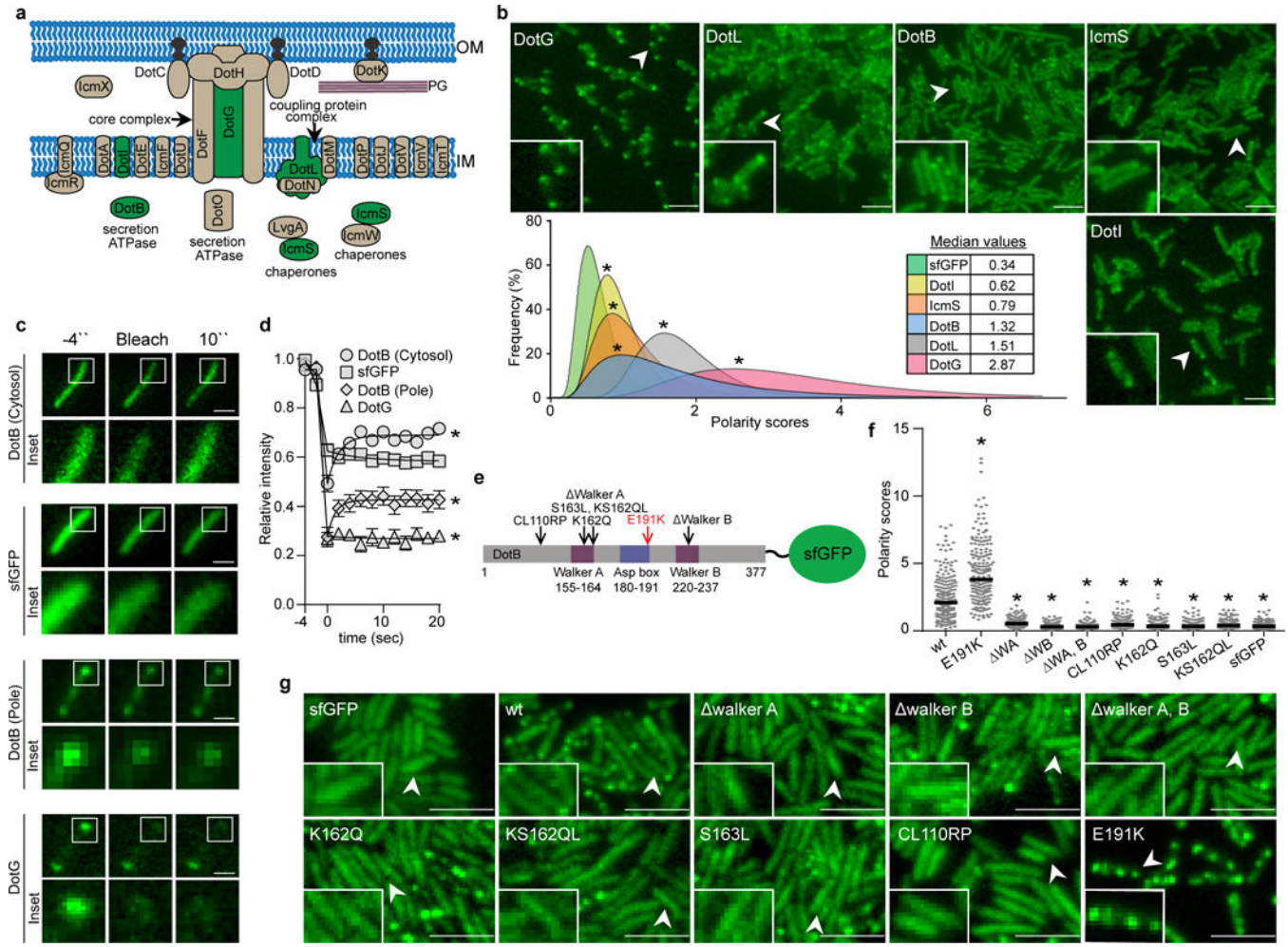

Fig. 1. ATP-bound DotB displays static polar localization

(a) Schematic model depicting Dot/Icm subunits tagged with sfGFP (green filling). **(b)** Real-time visualization with fluorescence light microscopy of DotG-sfGFP, DotL-sfGFP, DotB-sfGFP, IcmS-sfGFP and DotI-sfGFP. The abundance of Dot/Icm fusion proteins at the poles is displayed as frequency curves. Median values of the polarity scores are presented. Significance was calculated in comparison to sfGFP expressed from *dotB* operon. Scale bar, 3 μm. **(c)** Representative images of bacterial cells expressing sfGFP or the indicated Dot proteins tagged with sfGFP. Images of a cell with polar-localized DotB-sfGFP (Pole) and cytosolic DotB-sfGFP (cytosol) are shown. Images were acquired before photobleaching (−4″), immediately after photobleaching (Bleach), and 10 seconds after photobleaching (10″). Scale bar, 1 μm **(d)** Graphs depict the average normalized fluorescence intensity from FRAP experiments and results are presented as means ± SEM at every time point. Significance was calculated in comparison to sfGFP expressed from *dotB* operon. **(e)** Schematic model depicting DotB-sfGFP fusion protein with the locations of point mutations that were analyzed. Point mutations that reduce ATP binding are marked with black arrows. The E191K mutation conferring enhanced ATP binding without hydrolysis is marked with a red arrow. **(f)** Each dot represents the polarity score for individual bacteria producing sfGFP or the indicated DotB-sfGFP protein expressed from the endogenous location on the

chromosome. ΔWA and ΔWB represent Walker A and Walker B motifs deletions respectively. The black horizontal lines represent the medians of the polarity scores. Significance was calculated in comparison to DotB-sfGFP. **(g)** Real-time visualization of native and mutant forms of DotB-sfGFP or sfGFP. Scale bar, 3 μm. Samples sizes (n), significance values (*p*) and the type of statistical test used to calculate the significance in panels **b**, **d** and **f** are shown in Supplementary information Table 2.

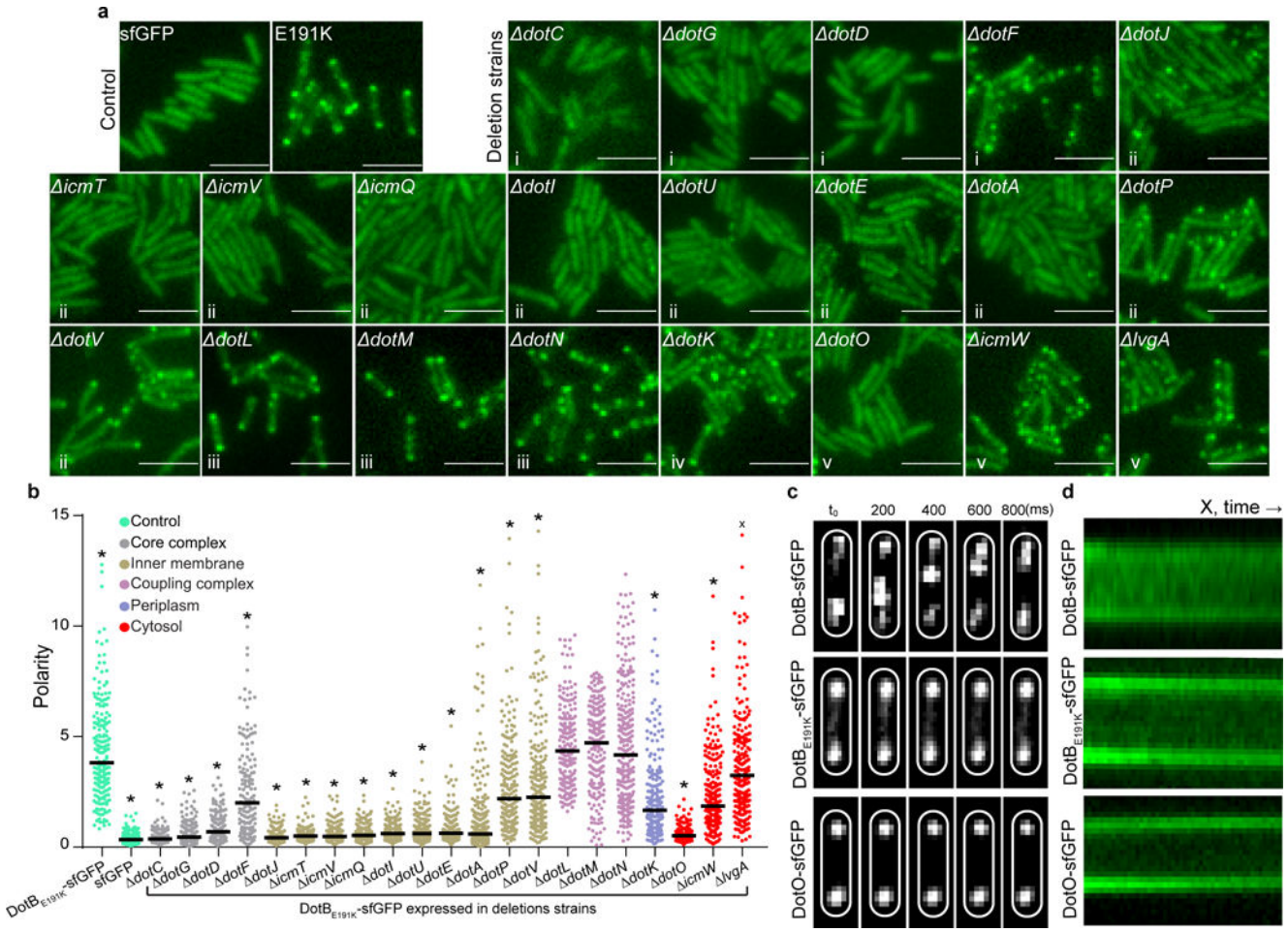

Fig. 2. The ATPase DotO is essential for polar recruitment of DotB

(a) Real-time visualization of $DotB_{E191K}$-sfGFP expressed in mutants deficient in the indicated Dot or Icm components. Deletion strains were grouped according to the following subcomplexes or cellular locations: core complex (i), inner membrane (ii), coupling protein complex (iii), periplasm (iv) and cytosol (v). sfGFP was expressed from *dotB* operon and served as a control. Scale bar, 3μm. **(b)** The polarity scores of $DotB_{E191K}$-sfGFP in the indicated deletion strains. The black horizontal lines represent the medians of the polarity scores. Significance was calculated in comparison to $DotB_{E191K}$-sfGFP. **(c)** Representative images from 4 independent experiments of DotB-sfGFP, $DotB_{E191K}$-sfGFP and DotO-sfGFP fluorescence shown at selected time points (200, 400, 600 and 800 milliseconds). Images were acquired using a motorized spinning disc confocal microscope and were restored by the NearestNeighbors deconvolution algorithm [32] of SlideBook™. **(d)** Representative Kymographs from 4 independent experiments of DotB-sfGFP, $DotB_{E191K}$-sfGFP and DotO-sfGFP fluorescence over time. Samples sizes (n), significance values (*p*) and the type of statistical test used to calculate the significance in panel **b** are shown in Supplementary information Table 2.

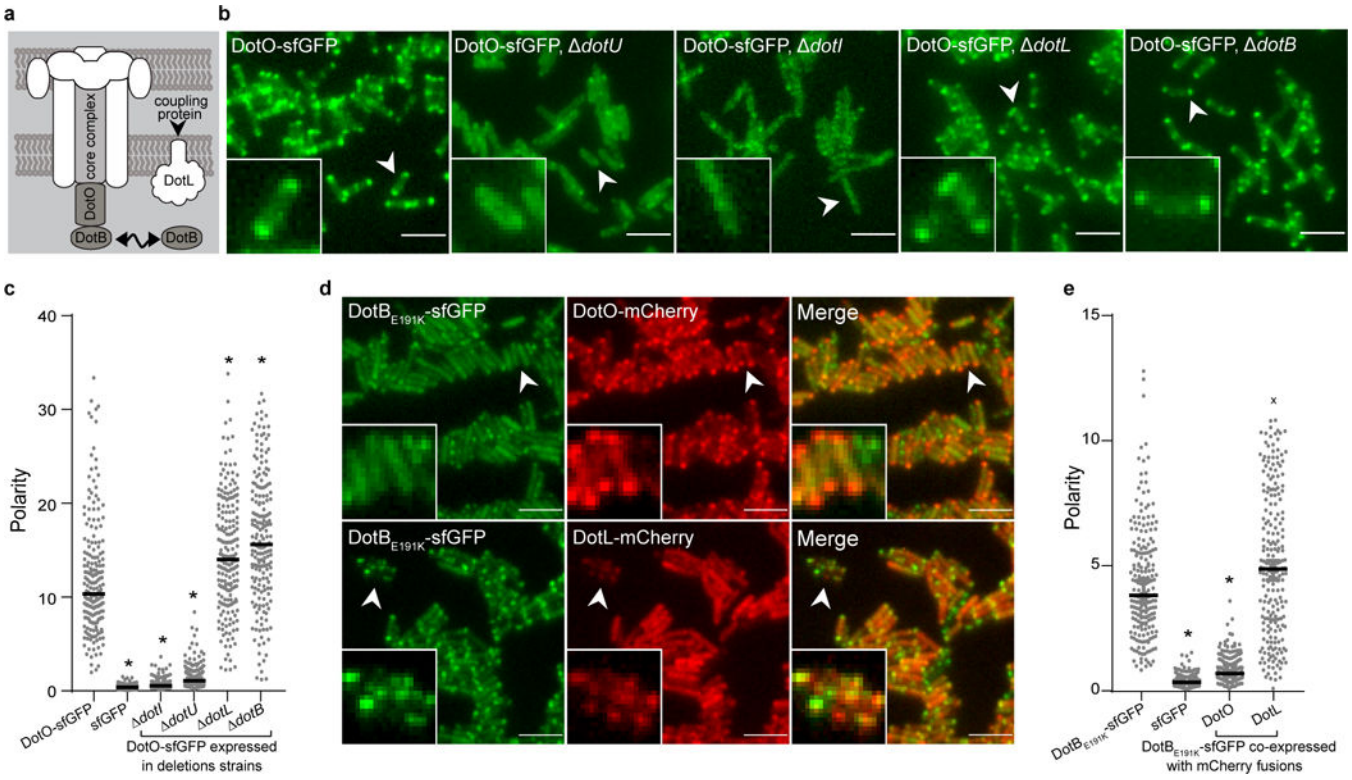

Fig. 3. The ATPase DotO is placed above DotB

(a) Model summarizing the hierarchy of DotO and DotB recruitment to the poles. Both proteins require the Dot/Icm machine (CC and IMC) for polar recruitment. DotB requires DotO for polar recruitment. DotL is not required for recruitment of DotO or DotB to the polar complex. **(b)** Real-time visualization of DotO-sfGFP expressed in strains having the indicated *dot* genes deleted **(c)** The polarity scores of DotO-sfGFP in strains having the indicated *dot* genes deleted. The black horizontal lines represent the medians of the polarity scores. Significance was calculated in comparison to DotO-sfGFP. **(d)** Real-time visualization of DotB$_{E191K}$-sfGFP co-expressed with DotO-mCherry or DotL-mCherry. Scale bar, 3μm. (e) The polarity scores of DotBE191K-sfGFP co-expressed with DotO-mCherry or DotL-mCherry. The black horizontal lines represent the medians of the polarity scores. Significance was calculated in comparison to DotBE191K-sfGFP. Samples sizes (n), significance values (p) and the type of statistical test used to calculate the significance in panels **c** and **e** are shown in Supplementary information Table 2.

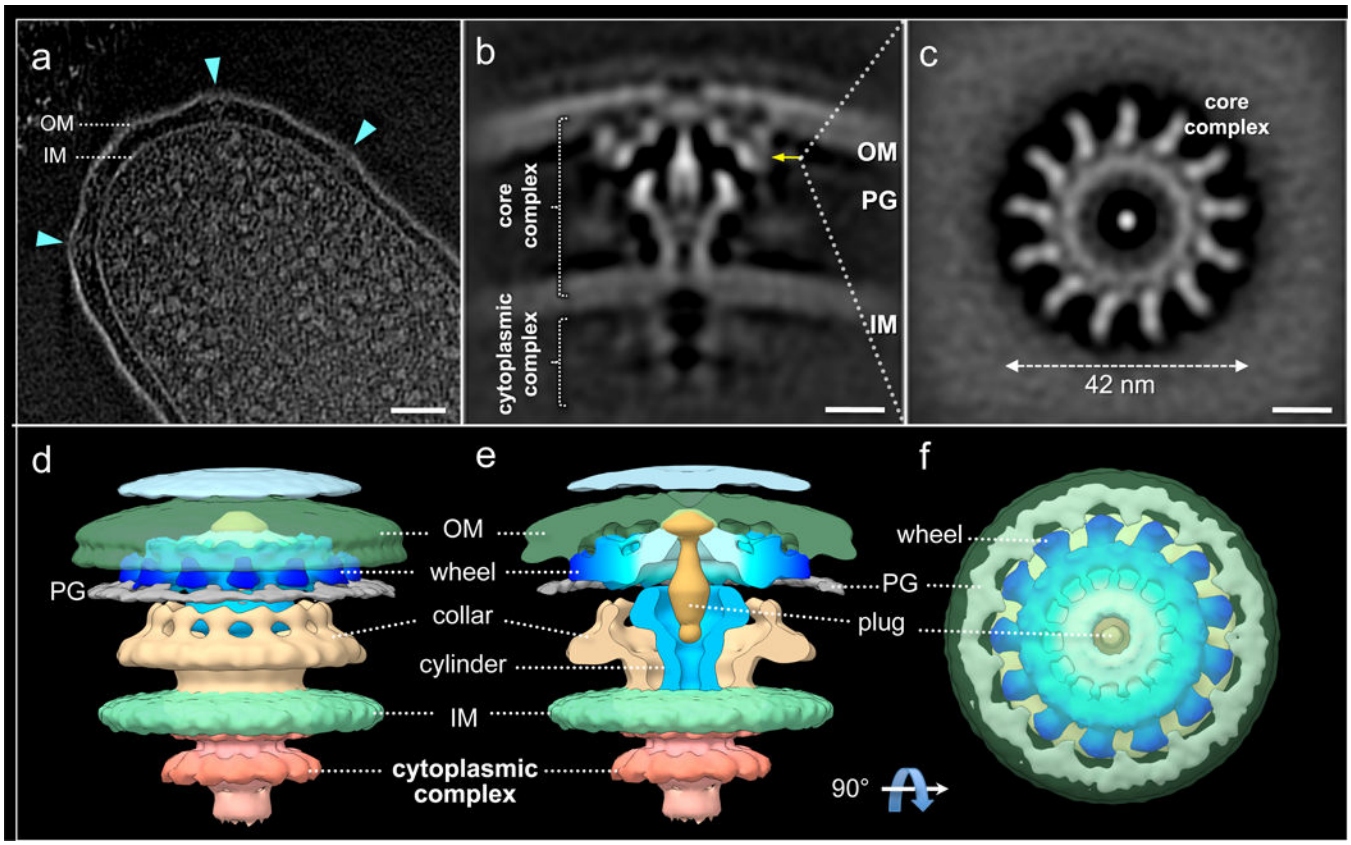

Fig. 4. *In situ* structure of the Dot/Icm type IVB secretion machine revealed by cryo-ET and sub-tomogram averaging

(a) A tomographic slice from a representative *L. pneumophila* cell showing multiple Dot/Icm machines embedded in the cell envelope. Scale bar, 100nm. **(b)** A central section through longitudinal plane of a global average structure *in situ* showing the components of the type IVB machine in the context of the outer membrane (OM), the peptidoglycan (PG), and the inner membrane (IM). Scale bar, 10nm. **(c)** Cross-section at the position indicated (B, yellow arrow) showing 13-fold symmetric features of the OMCC. Scale bar, 10nm. **(d)** and **(e)** 3-D surface rendering of the intact Dot/Icm machine showing the architecture of the OMCC, composed of a wheel-like structure incorporated in the OM, a plug, a central hollow cylinder, and a surrounding collar. **(f)** A top view showing the 13-fold symmetry of the wheel.

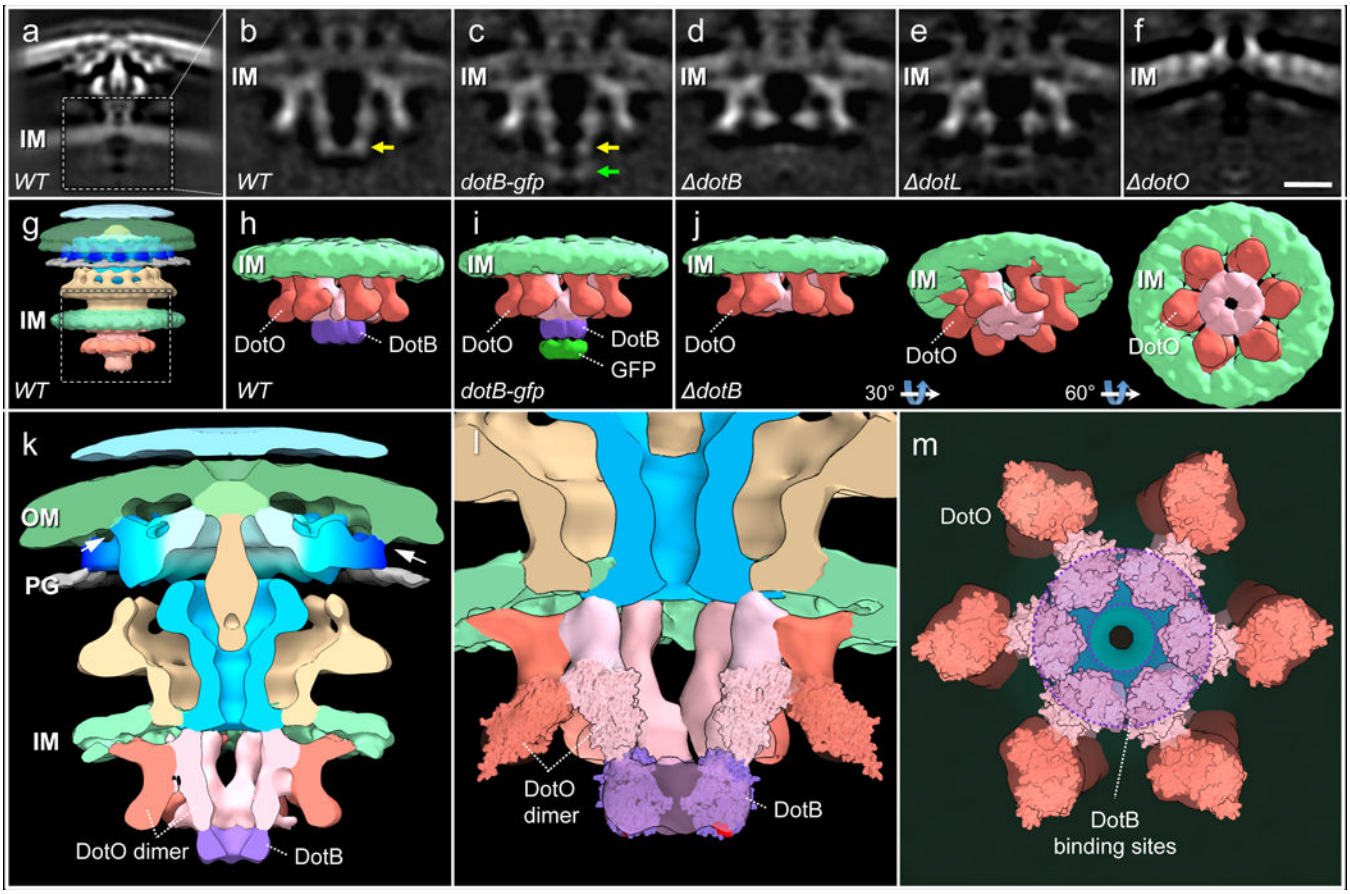

Fig. 5. The cytoplasmic complex, showing 6-fold symmetry, composed of ATPases DotO and DotB

The cytoplasmic complex boxed in **(a)** was locally refined **(b). (c)** A reconstruction from a DotB-GFP fusion mutant, with densities corresponding to DotB (yellow arrow, see also panel B) and sfGFP (green arrow). **(d)** A reconstruction from a Δ*dotB* mutant showing the absence of density at the bottom of the inverted V structures (compare with panel **b**). **(e)** A reconstruction from a Δ*dotL* mutant showing no major differences compared with native T4SS (compare with panel **b**). **(f)** A Δ*dotO* mutant lacks the entire cytoplasmic complex. Scale bar, 10nm. 3-D surface renderings of: **(g)** the entire Dot/Icm T4SS, **(h)** cytoplasmic complex in side view, **(i)** side view showing DotB and sfGFP, **(j)** DotO hexamer of dimers in side, angled and bottom views, **(k)** cut-away view of entire Dot/Icm T4SS, **(l** and **m)** docking of 12 pseudo DotO C-terminal structures into the map shown as side and bottom views; a hexamer of DotB (using the homolog PilT, PDB 3JVV) was fitted into the distal short cylinder and the C terminal residues were colored in red **(l)**.